
Edge-based anisotropic mesh adaptation for CFD applications

T. Coupez¹, G. Jannoun², J. Veysset³, and E. Hachem⁴

¹ MINES ParisTech, UMR CNRS 7635, BP 207, 06904 Sophia-Antipolis, France
thierry.coupez@mines-paristech.fr

² MINES ParisTech, UMR CNRS 7635, BP 207, 06904 Sophia-Antipolis, France
ghina.el-jannoun@mines-paristech.fr

³ MINES ParisTech, UMR CNRS 7635, BP 207, 06904 Sophia-Antipolis, France
jeremy.veysset@mines-paristech.fr

⁴ MINES ParisTech, UMR CNRS 7635, BP 207, 06904 Sophia-Antipolis, France
elie.hachem@mines-paristech.fr

Summary. This paper presents an anisotropic mesh adaptation technique relying on the length distribution tensor approach and an edge based error estimator. It enables to calculate a stretching factor providing a new edge length distribution, its associated tensor and the corresponding metric. The optimal stretching factor field is obtained by solving an optimization problem under the constraint of a fixed number of nodes. It accounts for different component fields in a single metric. With such features, the method proves to be simple and efficient and can be easily applied to a large panel of challenging CFD applications.

1 INTRODUCTION

Despite the increasing computer performances and the progress of computational fluid dynamics (CFD) in modelling and simulating time dependent physical phenomena, numerical restrictions caused mainly by the complexities of the simulations are still present.

Researchers are continuously investigating possible numerical strategies to resolve this problem while maintaining a good level of accuracy and a reasonable computational cost.

Anisotropic mesh adaptation has proved to be a powerful strategy to improve the quality and efficiency in particular of finite element/volume methods. It enables the capture of scale heterogeneities that can appear in numerous physical or mechanical applications including those having boundary layers, shock waves, edge singularities and moving interfaces ([1], [2], [3], [4], [5]). These adaptive techniques allow the creation of extremely stretched and highly directional elements which are key requirements for many CFD applications including Fluid-Structure Interaction (FSI), Multiphase flows and

Mutliphysics problems. Moreover, they provide a good level of accuracy within a reasonable degree of freedom.

Several approaches to build unstructured anisotropic adaptive meshes are often based on local modifications ([6], [7], [8], [9]) of an existing mesh. In fact, it mainly requires extending the way to measure lengths following the space directions and can be done by using a metric field to redefine the geometric distances. In parallel, theories of anisotropic a posteriori error estimation (*i.e.* [10]) have been well developed, leading to some standardization of the adaptation process; production of metrics from the error analysis of the discretization error and steering of remeshing by these metrics.

It follows that most adaptive anisotropic meshing techniques take a metric map as input. In practice, it is preferable to have a nodal metric map. Indeed, during the remeshing operations, the elements are much more volatile than the mesh nodes and therefore defining fields on a continuous basis ease their reconstruction, interpolation or extrapolation.

The author in [1] has adopted a different route for the metric construction. The latter is done directly at the node of the mesh without any direct information from the element, neither considering any underlying interpolation. It is performed by introducing a statistical concept: the length distribution function. A second order tensor was employed to approximate the distribution of lengths defined by gathering the information from the edges onto the node. Using such a technique, the error is computed along and in the direction of each edge.

In this work, we pursue further the approach developed in [1]. Rather than considering several metric intersections as in [2], [3], [4], and thus having much computations to perform, we propose in here to construct a single metric field. The latter takes into account multicomponent fields (tensors, vectors, scalars) characterizing the structure and the physics of the problem. These can include for instance the velocity norm, the velocity components, the temperature field and the Level-Set function.

Other features of the proposed anisotropic mesh adaptation technique are its automaticity and its independence from the problem at hand. It works under the constraint of a fixed degree of freedom to provide a desired level of accuracy while maintaining a low computational cost. With such advantages, we show in this paper that the proposed approach is general and very useful for approximating the solution of various Computational Fluid Dynamic (CFD) problems including flows at high Reynolds number [11]. The numerical examples show that it is well adapted to automatically capture all vortices, flow detachments, boundary/interior layers and moving interfaces.

The paper is structured as follows: we retrace in section 2 the main steps of the node based metric framework and describe the anisotropic mesh adaptation procedure governed by the length distribution tensor. In section 3, we provide some 2D and 3D numerical results showing the applicability and efficiency of the new highly parallelized anisotropic mesh adaptation.

2 Anisotropic mesh adaptation

We follow the lines of [1] to present an *a posteriori* error estimate based on the length distribution tensor approach and the associated edge based error analysis. In this work, we emphasis the application of this technique to different CFD problems.

2.1 Edge based error estimation

We consider a variable $u \in \mathcal{C}^2(\Omega) = \mathcal{V}$ and \mathcal{V}_h a simple P^1 finite element approximation space:

$\mathcal{V}_h = \{w_h \in \mathcal{C}^0(\Omega), w_h|_K \in P^1(K), K \in \mathcal{K}\}$ where $\Omega = \bigcup_{K \in \mathcal{K}} K$ and K is a simplex (segment, triangle, tetrahedron, ...).

We define $\mathbf{X} = \{\mathbf{X}^i \in \mathbb{R}^d, i = 1, \dots, N\}$ as the set of nodes of the mesh and we denote by U^i the nodal value of u at \mathbf{X}^i and we let Π_h be the Lagrange interpolation operator from \mathcal{V} to \mathcal{V}_h such that: $\Pi_h u(\mathbf{X}^i) = u(\mathbf{X}^i) = U^i, \forall i = 1, \dots, N$. As shown in figure 1, we denote the set of nodes connected to node i by $\Gamma(i) = \{j, \exists K \in \mathcal{K}, \mathbf{X}^i, \mathbf{X}^j \text{ are nodes of } K\}$.

By introducing the notation: $\mathbf{X}^{ij} = \mathbf{X}^j - \mathbf{X}^i$ and using the analysis carried in [1], we can set:

$$\nabla u_h \cdot \mathbf{X}^{ij} = U^{ij}, \quad (1)$$

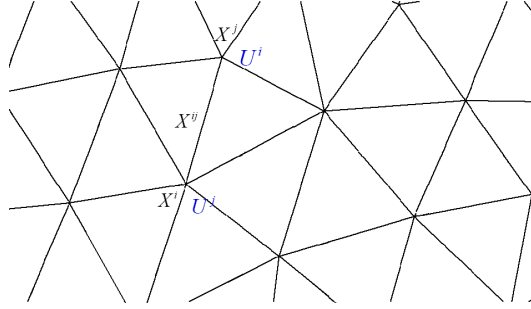


Fig. 1. Length \mathbf{X}^{ij} of the edge joining nodes i and j .

$$\| \underbrace{\nabla u_h \cdot \mathbf{X}^{ij}}_{U^{ij}} - \nabla u(\mathbf{X}^i) \cdot \mathbf{X}^{ij} \| \leq \max_{\mathbf{Y} \in [\mathbf{X}^i, \mathbf{X}^j]} |H(u)(\mathbf{Y}) \mathbf{X}^{ij} \cdot \mathbf{X}^{ij}|, \quad (2)$$

where $H(u) = \nabla^{(2)}u$ is the associated Hessian of u . Recall that taking $u \in \mathcal{C}^2(\Omega)$ we obtain $\nabla u \in \mathcal{C}^1(\Omega)$.

Applying the interpolation operator on ∇u together with (1) we obtain a definition of the projected second derivative of u in terms of only the values of the gradient at the extremities of the edge:

$$\nabla \mathbf{g}_h \mathbf{X}^{ij} \cdot \mathbf{X}^{ij} = \mathbf{g}^{ij} \cdot \mathbf{X}^{ij}, \quad (3)$$

where $\mathbf{g}_h = \Pi_h \nabla u$, $\mathbf{g}^i = \nabla u(\mathbf{X}^i)$ and $\mathbf{g}^{ij} = \mathbf{g}^j - \mathbf{g}^i$. Using a mean value argument, we set that: $\exists \mathbf{Y} \in [\mathbf{X}^i, \mathbf{X}^j] | \mathbf{g}^{ij} \cdot \mathbf{X}^{ij} = H(u)(\mathbf{Y}) \mathbf{X}^{ij} \cdot \mathbf{X}^{ij}$.

We use this projection as an approximation of the error along the edge:

$$e_{ij} = \mathbf{g}^{ij} \cdot \mathbf{X}^{ij}. \quad (4)$$

However this equation cannot be evaluated exactly as it requires knowing the gradient of u and also its continuity at the nodes of the mesh. For that reason, we resort to a gradient recovery procedure.

2.2 Gradient Recovery

Based on an optimization analysis, the author in [1] proposes a recovery gradient operator defined by:

$$\mathbf{G}^i = (X^i)^{-1} \sum_{j \in \Gamma(i)} U^{ij} \mathbf{X}^{ij}, \quad (5)$$

where $X^i = \frac{d}{|\Gamma(i)|} \sum_{j \in \Gamma(i)} \mathbf{X}^{ij} \otimes \mathbf{X}^{ij}$ is what we call the length distribution tensor at node \mathbf{X}^i . Note that this construction preserves the second order: $|(\mathbf{G}^i - \mathbf{g}^i) \cdot \mathbf{X}^{ij}| \sim (H(u) \mathbf{X}^{ij} \cdot \mathbf{X}^{ij})$ where \mathbf{G}^i is the recovery gradient at node i (given by (5)) and \mathbf{g}^i being the exact value of the gradient at node i . The approximated error is evaluated by substituting \mathbf{G} by \mathbf{g} in (4):

$$e_{ij} = \mathbf{G}^{ij} \cdot \mathbf{X}^{ij}.$$

2.3 Metric construction from the edge distribution tensor

Taking into account this error analysis, we construct the metric for the unit mesh as follows:

$$M^i = \left(\frac{d}{|\Gamma(i)|} \sum_{j \in \Gamma(i)} \mathbf{X}^{ij} \otimes \mathbf{X}^{ij} \right)^{-1}.$$

For a complete justification of this result, the reader is referred to [1].

2.4 Error behavior due to varying the edge length

We examine now how the error behaves when the length of the edges changes by stretching coefficients $s_{ij} \in \mathcal{S}$ defined by :

$$\mathcal{S} = \{s_{ij} \in R^+, i = 1, \dots, N, j = 1, \dots, N, \Gamma(i) \cap \Gamma(j) \neq \emptyset\}.$$

To obtain a new metric depending on the error analysis, a new length for each edge has to be calculated and then used for rebuilding the length distribution tensor. An interesting way of linking the error variations to the changes in edge lengths is done by introducing a stretching factor $s \in R^+$ such that

$$\begin{cases} \widetilde{\mathbf{X}}^{ij} = s\mathbf{X}^{ij} \\ ||\widetilde{e}_{ij}|| = s^2||e_{ij}|| = s^2||\mathbf{G}^{ij} \cdot \mathbf{X}^{ij}|| \end{cases} \quad (6)$$

where \widetilde{e}_{ij} and $\widetilde{\mathbf{X}}^{ij}$ are the target error at edge ij and its associated edge length respectively.

Following the lines of [1] we can simply define the metric associated with \mathcal{S} by:

$$\widetilde{M}^i = \frac{|\Gamma(i)|}{d} \left(\widetilde{X}^i \right)^{-1}, \quad (7)$$

where $\widetilde{X}^i = \frac{d}{|\Gamma(i)|} \sum_{j \in \Gamma(i)} s_{ij}^2 \mathbf{X}^{ij} \otimes \mathbf{X}^{ij}$ is the length distribution tensor and $|\Gamma(i)|$ is the cardinal of $\Gamma(i)$. Let n_{ij} be the number of created nodes in relation with the stretching factor s_{ij} and along the edge ij . When scaling the edges by a factor s_{ij} , the error changes quadratically so that the number of created nodes along the edge ij is given by:

$$n_{ij} = \left(\frac{\widetilde{e}_{ij}}{e_{ij}} \right)^{-\frac{1}{2}} = s_{ij}^{-1}.$$

As per node i , the created nodes along the different edge directions is given by the following tensor:

$$N^i = \left(\frac{d}{|\Gamma(i)|} \sum_{j \in \Gamma(i)} n_{ij} \frac{\mathbf{X}^{ij}}{|\mathbf{X}^{ij}|} \otimes \frac{\mathbf{X}^{ij}}{|\mathbf{X}^{ij}|} \right).$$

So that the total number of created nodes per node i is:

$$n^i = \det \left(\frac{d}{|\Gamma(i)|} \sum_{j \in \Gamma(i)} n_{ij} \frac{\mathbf{X}^{ij}}{|\mathbf{X}^{ij}|} \otimes \frac{\mathbf{X}^{ij}}{|\mathbf{X}^{ij}|} \right).$$

By considering the averaging process of the number of nodes distribution function, the total number of nodes in the adapted mesh is given by

$$N = \sum_i n^i.$$

A direct relation between N and e , assuming a uniform totally balanced error along the edge $\widetilde{e}_{ij} = e = \text{constant}$, is given by:

$$n^{ij}(e) = s_{ij}^{-1}(e) = \left(\frac{e}{e_{ij}} \right)^{-\frac{1}{2}}.$$

Hence, for a node i we have

$$n^i(e) = e^{-\frac{d}{2}} \det \left(\frac{d}{|I(i)|} \sum_{j \in I(i)} \left(\frac{1}{e_{ij}} \right)^{-\frac{1}{2}} \frac{\mathbf{X}^{ij}}{|\mathbf{X}^{ij}|} \otimes \frac{\mathbf{X}^{ij}}{|\mathbf{X}^{ij}|} \right) \Leftrightarrow n^i(e) = e^{-\frac{d}{2}} n^i(1),$$

so that

$$N = e^{-\frac{d}{2}} \sum_i n^i(1).$$

Therefore, the global induced error for a given total number of nodes N can be determined by:

$$e(N) = \left(\frac{N}{\sum_i n^i(1)} \right)^{-\frac{2}{d}}.$$

Thus, the corresponding stretching factors under the constraint of a fixed number of nodes N are given by:

$$s_{ij} = \left(\frac{e}{e(N)} \right)^{-\frac{1}{2}} = \left(\frac{\sum_i n^i(1)}{N} \right)^{\frac{2}{d}} e_{ij}^{-1/2}.$$

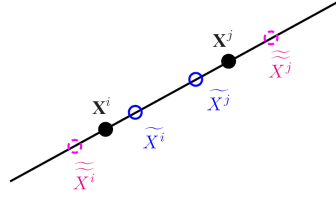


Fig. 2. Varying the edge in its own direction.

2.5 Extension to multi-component field

Here we propose to construct a unique metric directly from a multi-component vectors field containing, for instance, all the components of the velocity field and/or different level-set functions. Consequently, we do not need to intersect several metrics but to construct it using the following error vector $\mathbf{e}_{ij} = \{e_{ij}^1, e_{ij}^2, \dots, e_{ij}^n\}$ where n is the number of components. Let $u = \{u_1, u_2, \dots, u_n\}$, $\mathcal{Z} = \mathcal{V}^n$ and $\mathcal{Z}_h = \mathcal{V}_h^n$. In the view of constructing a unique metric, the above theory is applied for each component of u . It comes out immediately that the error is now a vector given by: $\vec{e}_{ij} = \{e_{ij}^1, e_{ij}^2, \dots, e_{ij}^n\}$ and then

$$s_{ij} = \left(\frac{\|e(N)\|}{\|\vec{e}_{ij}\|} \right)^{\frac{1}{2}}.$$

Here, the norm can be the discrete L_2 , L_1 or L_∞ norms.

For illustration, we combine into one global vector, both the level-set function and all components of the velocity field.

Denote by v_h the finite element solution of the Navier Stokes equations and $\Pi_h v$ its interpolant. In general, we have that

$$\exists c > 0, \quad \|v_h - v\| \leq c \|\Pi_h v - v\|.$$

Let $v_h(X^i) = V^i \in R^d$, $d = 2, 3$ and $\mathcal{Y} = \left(\frac{v}{|v|}, |v|, \alpha \right)$ be the vector field made of $d + 1$ components vector fields, with α the level-set function used to localize a fluid-fluid or fluid-solid interfaces. We obtain for every node i ,

$$\Pi_h \mathcal{Y}(\mathbf{X}^i) = \left(\frac{V^i}{|V^i|}, |V^i|, \alpha \right) = \mathcal{Y}^i.$$

Figure 3 shows a 2D adapted mesh obtained for the flow behind an airfoil profile. The adaptation takes into account the velocity field (components and norm) as well as the Level-Set function. As expected, it renders extremely stretched elements along the fluid-solid interface and follows the components of the velocity field. It shows the correct orientation and deformation of the mesh elements.

3 CFD applications

In this section, we present several numerical examples to illustrate the flexibility of the approach dealing with high Reynolds flows and mutli-domain problems having complex geometry. The numerical simulations were carried out using the C++ CimLib finite element library (see [12]).

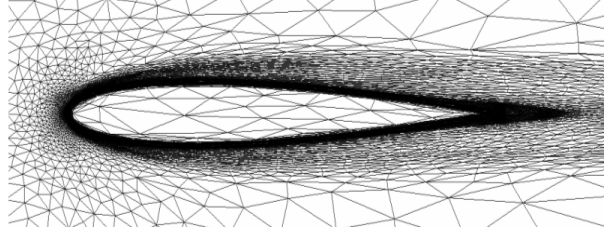


Fig. 3. Anisotropic refined fluid-solid interface of an immersed NACA0012.

3.1 Application to Incompressible flows at high Reynolds number

We begin to solve numerically the classical 2-D and 3-D lid-driven flow problems. This test has been widely used as a benchmark for numerical methods and has been analyzed by a number of authors [13, 14]. Homogenous Dirichlet boundary conditions for the velocity are imposed equal to one on the upper boundary of the computational domain, *i.e.* at $y = 1$, and zero elsewhere. The source term is set to zero. The viscosity is adjusted in order to obtain Reynolds number of 1,000, 5,000, 10,000, 20,000, and 100,000.

An important point to mention before we start is that the following mesh adaptations are always performed for a fixed number of nodes. This turns out to be an important advantage because it avoids a drastic increase in the number of unknowns and in the computational cost. Therefore, for Reynolds number of 1000, 5000 and 10,000 we fixed the number of nodes N to be equal to 10,000 whereas, for Reynolds number 20,000 and 100,000 the number of nodes is set to 20,000. The adaptive process always starts from the uniform mesh and is iterated every five time steps.

The results on the five respective meshes can be seen in Figure 4. Note the concentration of the resolution not only along all the boundary layers but also at the detachment regions. This reflects well the anisotropy of the solution caused by the discontinuity of the boundary conditions and the nature of the flow. The elements at the central bulk of the cavity region around the primary vortex are mostly isotropic and increase in size as the Reynolds number increases. Again, this reflects and explains how, for a controlled number of nodes, the mesh is naturally and automatically coarsened in that region with the goal of reducing the mesh size around the secondary vortices in the bottom corners.

As the Reynolds number increases, the capturing of different secondary vortices is surprisingly very good. The zoom on the right side of the cavity in Figure 5 highlights how sharply the layers can be captured. It shows the correct orientation and deformation of the mesh elements (longest edges parallel to the boundary). This yields to a great reduction in the number of triangles. This results give confidence that the extension of the approach to take into

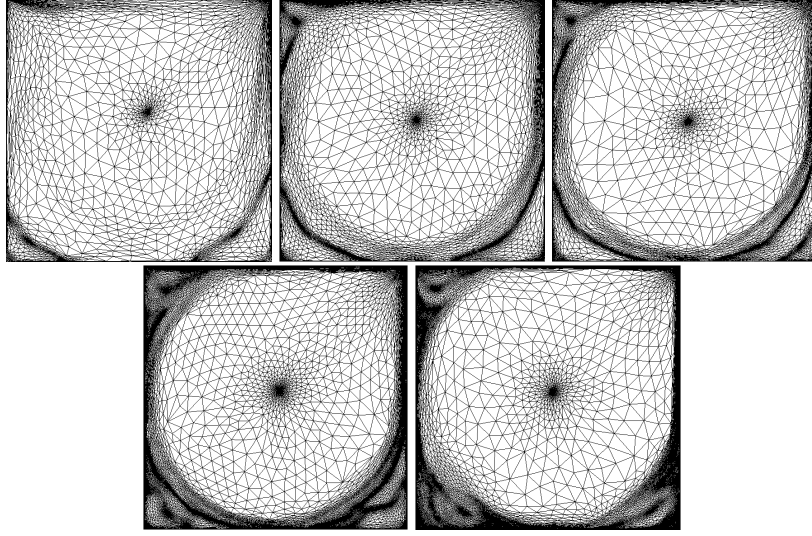


Fig. 4. Anisotropic meshes at Reynolds 1000, 5000, 10,000, 20,000 and 100,000

account all the velocity components holds very well and plays an important role for transient flows.

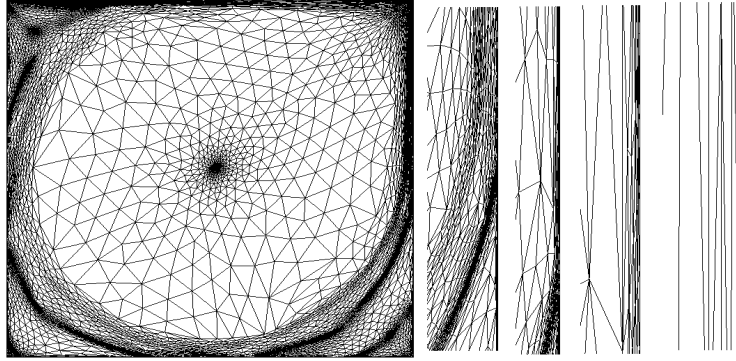


Fig. 5. Zooms on the mesh close to the right wall

For comparisons, we plot the velocity profiles for U_x along $x = 0.5$ and for U_y along $y = 0.5$ at Reynolds 10,000. Figure 6 shows respectively that the result is in very good agreement with a reference solution computed on a $600 \times 600 = 360,000$ points fixed mesh [13]. More results are presented and analyzed in [11].

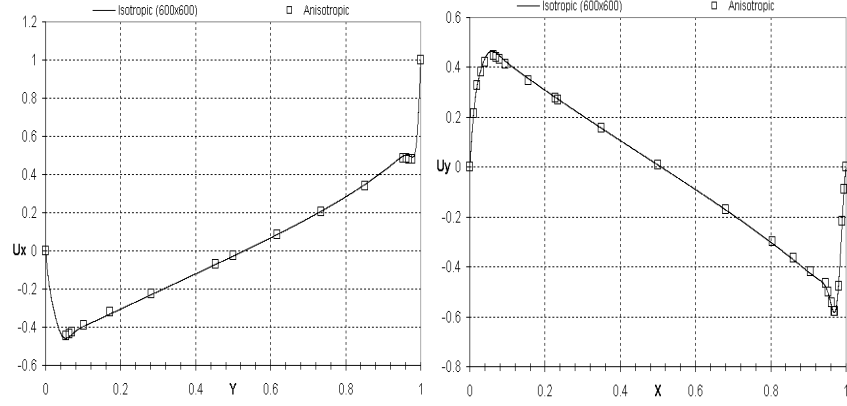


Fig. 6. Comparison of velocity profiles in the mid-planes for $Re = 10,000$. Left: Velocity profiles for U_x along $x = 0.5$. Right: Velocity profiles for U_y along $y = 0.5$.

We repeated the same experiments in 3-D for Reynolds numbers equal to 1000, 3200 and 5,000 respectively. The fixed number of elements is ($\sim 450,000$). Again, in 3-D where the flow characteristics are much more complicated, all the boundary layers as well as the vortices are sharply captured and identified as shown in figure 7.

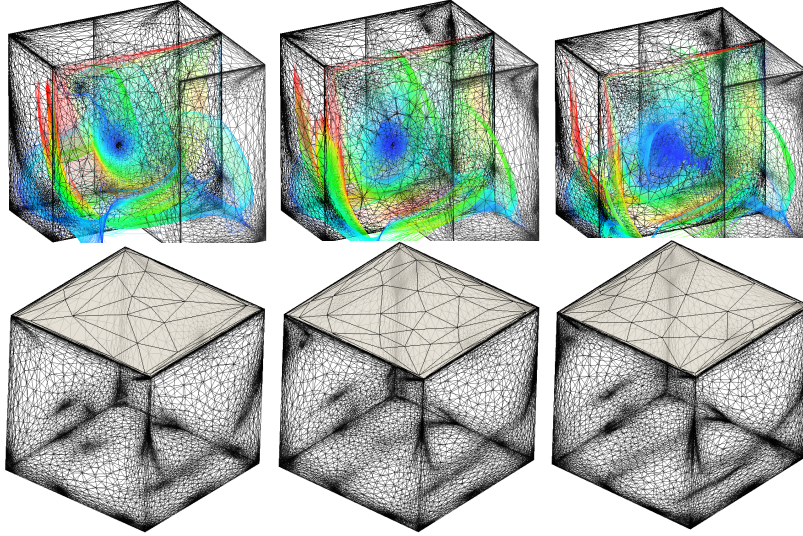


Fig. 7. Streamlines snapshots and the adapted meshes at Reynolds 1000, 32000 and 5000

In figure 8, we present different zoomed captures on the mesh to show how the elements can be highly stretched along the direction of the layers. This reflects well the accuracy and details of the resolution caused by the discontinuity of the boundary conditions and the nature of the flow.

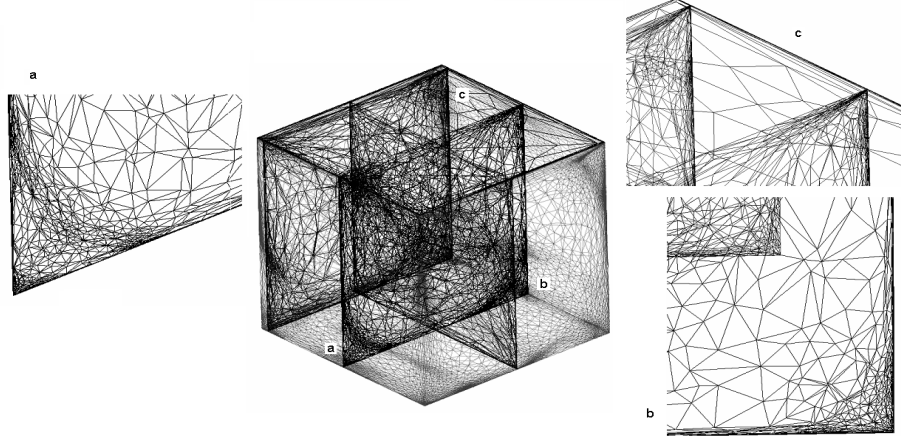


Fig. 8. Zooms on the mesh details inside the 3D cavity

3.2 Application to Fluid-Structure Interaction

We continue by investigating the flow around a NACA0012 airfoil in a channel [16]. This study is considered as an important step to investigate the feasibility of the proposed multicomponents feature. The purpose is to show the flexibility of the method to deal with a large variety of geometries. Rather than spending the effort on the mesh construction around the airfoil, we bypass this step and we consider the simplest rectangular domain. As mentioned before, the NACA profile will be represented by a simple distance function.

Therefore, we consider two cases. In the first one, we use the classical approach and we impose zero boundary conditions on the profile. So the effort will be concentrated on the geometry and on building the fluid mesh while well respecting the curvatures of the airfoil profile. In the second case, (i) we consider a large simple channel domain, (ii) we compute analytically the distance function of the NACA profile located at the center, (iii) we apply the anisotropic mesh adaptation, and finally, (iv) we mix and assign the physical properties. The obtained finite element meshes that are used in the two cases are depicted in figure 9.

We apply the same conditions on both test cases and we compare the solutions. The Reynolds number Re_∞ based on the cord c is equal to 5000

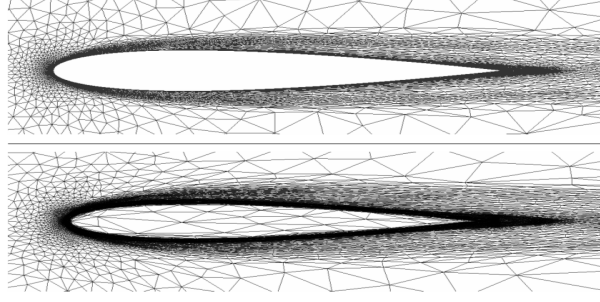


Fig. 9. Finite element meshes: only the fluid domain (up) - the air-NACA domain (bottom).

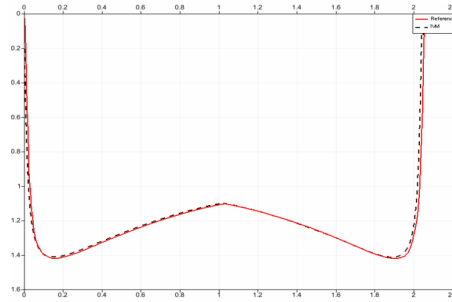


Fig. 10. Comparisons of drag coefficients. (-) reference, (\cdots) present work

and the angle of incidence is set to 0. The number of elements is fixed to 45000.

As the proposed *a posteriori* estimation combines the simultaneous adaptivity on the level-set scalar field and the velocity field, boundary layers and inner layers are automatically captured due to the anisotropically adapted mesh exhibiting highly stretched elements.

A comparison of the drag coefficients using the classical and the new approach is presented in figure 10. A very good agreement between the two numerical solutions is highlighted by the snapshots of the norm of the velocity, the pressure fields and the streamlines computed on the entire domain (fluid and structure) and on only the fluid domain in figures 11, 12 and 13 respectively.

3.3 Application to Immersed and Mutli-domain Approaches

Figure 14 and 15 present the parallel numerical simulation of unsteady flow around a 3D helicopter in forward flight. The mesh generation algorithm allows the creation of extremely anisotropic elements stretched along the inter-

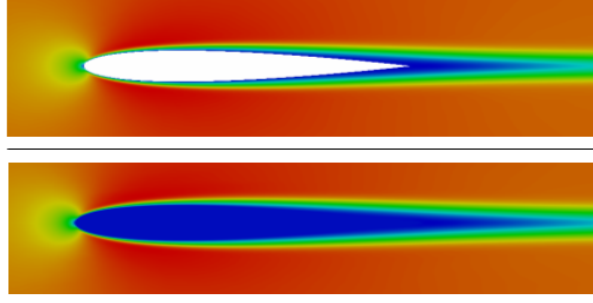


Fig. 11. Norm of the velocity calculated over the fluid domain (up) and the entire domain (bottom).

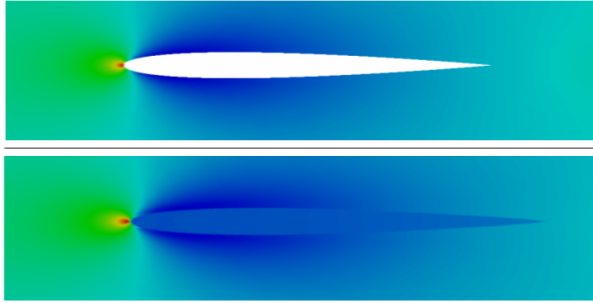


Fig. 12. Pressure distribution calculated over the fluid domain (up) and the entire domain (bottom).

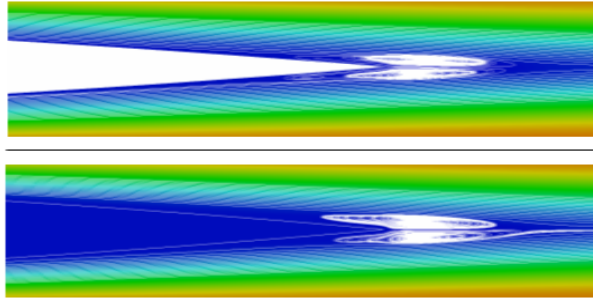


Fig. 13. Streamlines distribution calculated over the fluid domain (up) and the entire domain (bottom).

face, which is an important requirement for flows behind complex geometries. The final obtained mesh reflects the capability of the method to render a well respected geometry in terms of curvature, angles and complexity. Contrary to others techniques, this promising method can provide an alternative to body-fitted mesh for very complex geometry.

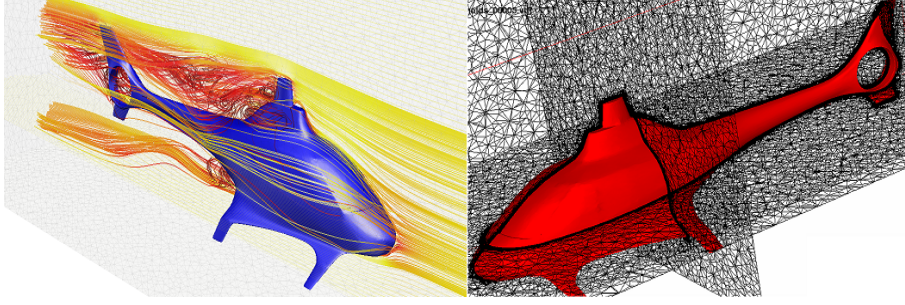


Fig. 14. Numerical simulation of unsteady flow around a helicopter in forward flight

This simulation is obtained using 96 2.4 Ghz Opteron cores in parallel (linked by an Infiniband network). The mesh consists of $\sim 1.6M$ tetrahedral elements and $\sim 300,000$ nodes. The purpose of this example is to confirm the motivation behind pursuing such general approach. Indeed, it allows to easily deal with a large diversity of complex shapes and dimensions without mesh reconstructions and to handle the interfaces through anisotropic mesh adaptation.

3.4 Application to 3D multiphase flows

In this section, three-dimensional simulation of the jet buckling phenomenon is presented. Fluid buckling occurs when a highly viscous fluid drops vertically towards a surface. This phenomenon is characterized by toroidal oscillations of the flow after its contact with the surface. We consider this free surface flow problem to demonstrate the efficiency and robustness of the numerical method in modelling three-dimensional unsteady two-phase flows with high density ratio.

The fluids are injected from 4 injectors at a two-meter height container. The diameter of the injectors is $0.05m$. Initially, we fill the container with the first fluid which is presented in yellow till it reaches the height of $0.3m$. The used viscosity is $368Pa.s$ and the density is $1770kg/m^3$. Once the first fluid reaches the prescribed height, the second one is then injected at the speed of $0.1m/s$ and falls under the gravity at $9.8m/s^2$. The second fluid, highlighted in green, has the same density as the first one, but slightly less viscous with a viscosity of $352Pa.s$. In this simulation, we fixed the number of nodes N to

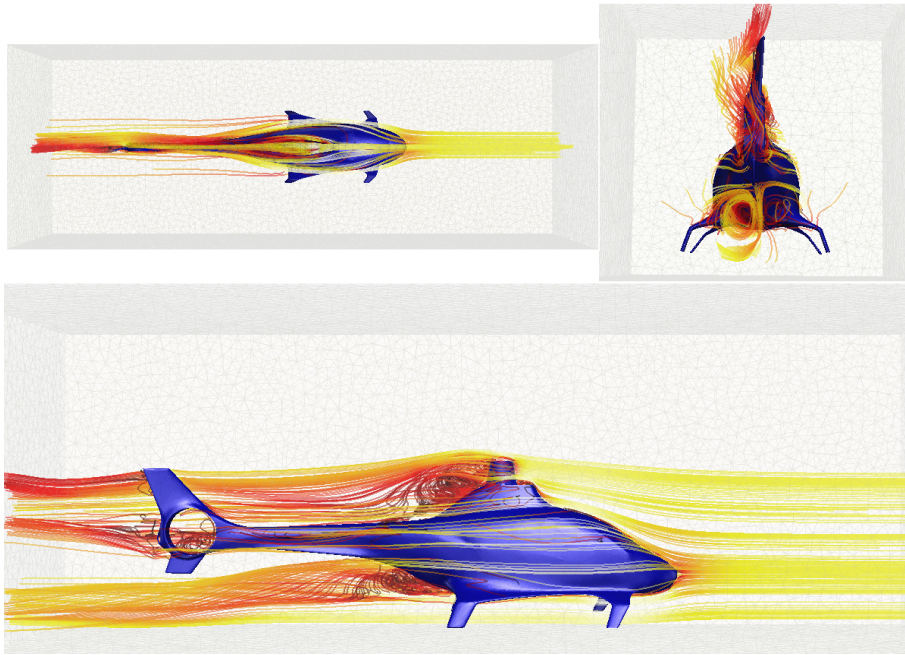


Fig. 15. Different snapshots of the flow around a helicopter in forward flight

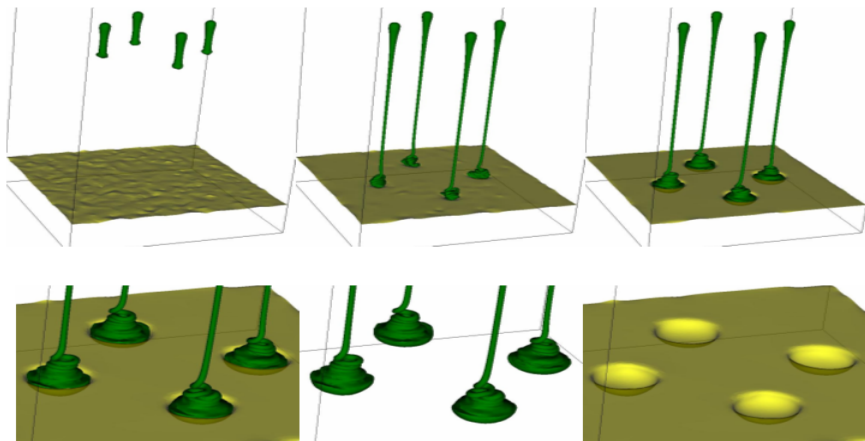


Fig. 16. The evolution of multi-fluid buckling phenomenon.

150,000. Recall that solving an optimization problem under the constraint of a fixed number of edges in the mesh offers an advantageous and useful tool for practical 3D simulation of multiphase flow dynamics. The calculation is executed on 32 processors during 2 days.

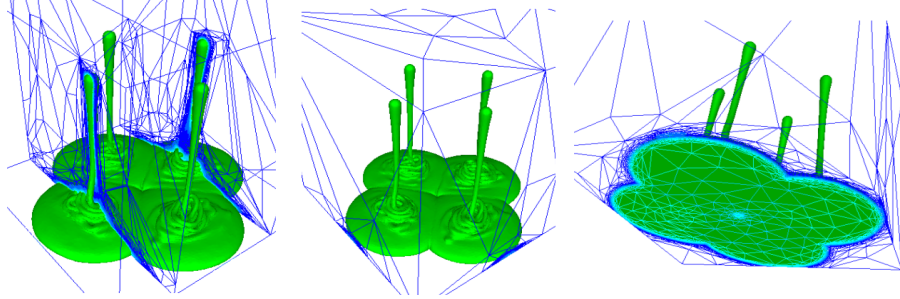


Fig. 17. Zoom on the anisotropic mesh with highly stretched elements at the interfaces.

As shown in figure 16, the evolution of the falling fluid appears very realistic rendering the fluid buckling phenomenon. In figure 17 we present different zoomed captures on the mesh to show how the elements can be highly stretched. This reflects well the accuracy and details of the resolution caused by the discontinuity and the nature of the flow. The anisotropic adaptive procedure modifies the mesh in a way that the local mesh resolutions become adequate in all directions. Again, this reflects and explains how, for a controlled number of nodes, the mesh is naturally and automatically coarsened far from the interfaces with the goal of reducing the mesh size around the multi-fluid buckling phenomenon.

4 Conclusion

We have shown in this paper that anisotropic adapted meshes with highly stretched elements is well adapted to challenging CFD applications with complex structure. The a posteriori error estimator is based on the length distribution tensor approach and the associated edge based error analysis. We proposed an important extension of the anisotropic theory to take into account multicomponent fields within a single metric. It was successfully addressed for the incompressible Navier-Stokes equations at high Reynolds numbers as well as for multi-domain problems. All the meshes are obtained by solving an optimization problem under the constraint of a fixed number of nodes. The method proves to be capable of automatically producing boundary layers, detecting all the main directional flow features and accurately capturing the interfaces. Further investigations will take into account the performance of the

presented adaptive method in terms of the computational cost, the speed-up and the frequency of remeshing.

References

1. Coupez T (2011) Metric construction by length distribution tensor and edge based error for anisotropic adaptive meshing. *Journal of Computational Physics* 230 2391-2405
2. Alauzet F (2003) Adaptation de maillage anisotrope en trois dimension. Applications aux simulations instationnaires en Mécanique des Fluides. Ph.D. thesis, school Université de Montpellier II, Montpellier
3. Frey P, Alauzet F (2005) Anisotropic mesh adaptation for CFD computations. *Computer Methods in Applied Mechanics and Engineering* 194 5068-5082
4. Alauzet F, Frey P, George P.L, Mohammadi B (2007) 3D transient fixed point mesh adaptation for time-dependent problems: Application to CFD simulations. *Journal of Computational Physics* 222 592-623
5. Gruau C, Coupez T (2005) 3D Tetrahedral, Unstructured and Anisotropic Mesh Generation with Adaptation to Natural and Multidomain Metric. *Computer Methods in Applied Mechanics and Engineering* 194 4951-4976
6. Coupez T (1994) A mesh improvement method for 3D automatic remeshing, *Numerical Grid Generation in Computational Fluid Dynamics and Related Fields*. Pineridge Press 615-626
7. Li X, Shephard M.S, Beall M.W (2005) 3D anisotropic mesh adaptation by mesh modification. *Computer Methods in Applied Mechanics and Engineering* 194 4915-4950
8. Shephard M.S, Flaherty J.E, Jansen K.E, Li X, Luo X, Chevaugeron N, Remacle J.F, Beall M.W, Obara R.M (2005) Adaptive mesh generation for curved-domains. *Applied Numerical Mathematics* 52 251-271
9. Remacle J.F, Li X, Shephard M.S, Flaherty J.E (2005) Anisotropic Adaptive Simulation of Transient Flows using Discontinuous Galerkin Methods. *International Journal for Numerical Methods in Engineering* 62 899-923.
10. Formaggia L, Perotto S (2001) New anisotropic a priori error estimate. *Numer. Math.* 89 641-667
11. Coupez T, Hachem E (2011) Solution of high Reynolds incompressible flow with stabilized finite element method and adaptive anisotropic meshing. submitted to *Computer Methods in applied Mechanics and Engineering*
12. Digonnet H, Coupez T (2003) Object-oriented programming for fast and easy development of parallel applications in forming processes simulation. In K.J. Bathe, editor, *Second MIT Conference on Computational Fluid and Solid Mechanics* 1922-1924
13. Hachem E, Rivaux B, Klozcko T, Digonnet H, Coupez T (2010) Stabilized finite element method for incompressible flows with high reynolds number. *Journal of Computational Physics* 229 8643-8665
14. Ghia U, Ghia K.N, Shin (1982) C.T High-Re solutions for incompressible flow using the Navier-Stokes equations and a multigrid method. *Journal of Computational Physics* 48 387-411
15. Albensoeder S, Kuhlmann H (2005) Accurate three-dimensional lid-driven cavity flow. *Journal of Computational Physics* 206 536-558

16. Pagnutti D, Olivier-Gooch C (2010) Two-dimensional Delaunay-based anisotropic mesh adaptation. *Engineering with Computers* 26 407-418